

Cr L-edge X-ray Absorption Spectroscopy of Cr^{III}(acac)₃ in Solution with Measured and Calculated Absolute Absorption Cross Sections

Markus Kubin^a, Meiyuan Guo^b, Maria Ekimova^c, Erik Källman^b, Jan Kern^d, Vittal K. Yachandra^d, Junko Yano^d, Erik T. J. Nibbering^{c,*}, Marcus Lundberg^{b,*}, Philippe Wernet^{a,*}

^aInstitute for Methods and Instrumentation for Synchrotron Radiation Research, Helmholtz-Zentrum Berlin für Materialien und Energie GmbH, 12489 Berlin, Germany.

^bDepartment of Chemistry - Ångström Laboratory, Uppsala University, SE-75121 Uppsala, Sweden.

^cMax-Born-Institut für Nichtlineare Optik und Kurzzeitspektroskopie, 12489 Berlin, Germany.

^dMolecular Biophysics and Integrated Bioimaging Division, Lawrence Berkeley National Laboratory, Berkeley, CA 94720, USA.

*Authors to whom correspondence should be addressed.

Philippe Wernet, Helmholtz-Zentrum Berlin, Albert-Einstein-Str. 15, 12489 Berlin, Germany, Tel: +49 30 806213448, email: wernet@helmholtz-berlin.de.

Marcus Lundberg, Uppsala University, SE-75121 Uppsala, Sweden, Tel: +46-18-4713708, email: marcus.lundberg@kemi.uu.se

Erik T. J. Nibbering, Max-Born-Institut für Nichtlineare Optik und Kurzzeitspektroskopie, 12489 Berlin, Germany. Tel: +49 30 63921477, email: nibberin@mbi-berlin.de

Abstract

X-ray absorption spectroscopy at the L-edge of 3d transition metals is widely used for probing the valence electronic structure at the metal site via 2p-3d transitions. Assessing the information contained in L-edge absorption spectra requires systematic comparison of experiment and theory. We here investigate the Cr L-edge absorption spectrum of high-spin chromium acetylacetonate $\text{Cr}^{\text{III}}(\text{acac})_3$ in solution. Using a transmission flatjet enables determining absolute absorption cross sections and spectra free from x-ray induced sample damage. We address the challenges of measuring Cr L absorption edges spectrally close to the O K absorption edge of the solvent. We critically assess how experimental absorption cross sections can be used to extract information on the electronic structure of the studied system by comparing our results of this $\text{Cr}^{\text{III}} (3d^3)$ complex to our previous work on L-edge absorption cross sections of $\text{Mn}^{\text{III}}(\text{acac})_3 (3d^4)$ and $\text{Mn}^{\text{II}}(\text{acac})_2 (3d^5)$. Considering our experimental uncertainties, the most insightful experimental observable for this $d^3(\text{Cr}^{\text{III}})$ - $d^4(\text{Mn}^{\text{III}})$ - $d^5(\text{Mn}^{\text{II}})$ series is the L-edge branching ratio and we discuss it in comparison to semi-empirical multiplet theory and ab-initio restricted active space calculations. We further discuss and analyze trends in integrated absorption cross sections and correlate the spectral shapes with the local electronic structure at the metal sites.

I. Introduction

X-ray absorption spectroscopy (XAS) at the L-edge of 3d transition metals is widely used for studying the local valence electronic structure at the metal center. As L-edge XAS probes the metal-centered $2p \rightarrow 3d$ transitions from the metal L (2p) shell to the unoccupied metal 3d-derived molecular orbitals,¹⁻³ the L-edge absorption spectra are sensitive to the spin state and the oxidation state of the metal center and to the local metal-ligand environment.⁴⁻⁹ However, the absorption energies and transition intensities are shaped by a multitude of interactions, which makes it demanding to systematically correlate spectra and local electronic structure of the complex. Still, there are general trends that are highly useful. For example, it is an accepted notion that for high-spin complexes the metal oxidation-state is expressed as a spectral shift in L-edge XAS.^{1, 4, 8, 10-11} Further, the integrated absorption cross section is proportional to the number of 3d holes and the metal-character of the 3d orbitals and the relative intensity of the L_3 and L_2 edges, split by 2p spin-orbit coupling, is sensitive to the spin state.¹² Finally, spectral shape can be used to get further details about metal-ligand interactions with the use of advanced theoretical methods.³

High-spin ionic acetylacetonato complexes are ideally suited systems to assess these observables in a systematic study. These complexes are composed as $M^X(\text{acac})_y$ where M^X denotes the metal ion with the formal oxidation state X and y denotes the number of $(\text{acac})^{-1}$ ligands. 3d transition metal acetylacetonates are available for $M = \text{V}, \text{Cr}, \text{Mn}, \text{Fe}, \text{Co}, \text{Ni}, \text{Cu}$ with metal oxidation states $X = \text{II}, \text{III}$, and they reflect important classes of metal-ligand symmetries, from tetrahedral ($y = 2$) to (Jahn-Teller distorted) octahedral ($y = 3$) metal-oxygen symmetry. Recent experimental and theoretical advances now enable new approaches to an unambiguous interpretation of L-edge XAS spectra of transition metal complexes. Liquid-jet sample delivery systems allow probing the sample in solution^{8, 13-14} thereby avoiding the influence of x-ray induced

sample damage of the high-valent systems by continuously replenishing the sample.^{8, 15-16} Novel ab initio restricted active space (RAS) calculations¹⁷⁻²⁰ combine descriptions of local atomic multiplet and ligand-field effects in the core-excited final states^{2-4, 6, 21-22} with treatment of orbital interactions thereby enabling to correlate L-edge XAS spectra with charge and spin densities at the metal site.

Here we use a fast-flowing liquid flat-jet system^{14, 23-24} to measure the Cr L-edge transmission XAS spectrum of Cr^{III}(acac)₃ in solution free of x-ray induced sample damage. Cr^{III}(acac)₃ has formally three Cr 3d electrons and a near octahedral CrO₆ core as found from crystallographic²⁵⁻²⁶ and UV-vis investigations,²⁷⁻²⁹ see Fig. 1A. As shown in Fig. 1B, the octahedral ligand field splits the metal 3d-orbitals into three singly occupied t_{2g} and two empty e_g orbitals. We compare the results from L-edge XAS of Cr^{III}(acac)₃ to our previous results on Mn^{III}(acac)₃ and Mn^{II}(acac)₂ (refs.^{11, 14}) with four (Mn^{III}) and five (Mn^{II}) 3d electrons. With data from this series, we analyze how the nominal number of metal 3d electrons, as well as the metal-ligand environment, can be correlated to the L-edge XAS spectra. The transmission mode makes it possible to analyze both integrated absorption cross sections, as well the L-edge branching ratios I(L₃)/I(L₃+L₂),¹² unaffected by state-dependent fluorescence yield.^{13, 30-31} Further information on electronic structure is obtained by a combination of semi-empirical crystal-field multiplet (CFM) and charge-transfer multiplet (CTM) calculations^{2-3, 21, 32} with RAS calculations. With these comparisons we provide new insights into the information content of L-edge XAS of these high-spin acetylacetonato M^X(acac)_y complexes.

II. Materials and Methods

Sample Preparation. $\text{Cr}^{\text{III}}(\text{acac})_3$ (Chromium(3+) tris[(2Z)-4-oxo-2-penten-2-olate]) was purchased as a crystalline powder (97% purity, ‘ACROS organics’) and was used without further purification. It was dissolved in ethanol abs. ($\geq 99.8\%$ purity, ‘Sigma-Aldrich’) with a concentration of 20 mM. The sample was filtered with ‘RC 0.45 μm ’ filters (‘Carl Roth’) before injection into vacuum. During sample preparation and sample injection, care was taken to minimize exposure to oxygen and ambient light. We note that for concentrations of $\text{Cr}^{\text{III}}(\text{acac})_3$ larger than 20 mM the transmission flatjet could not be sufficiently stabilized for measurements in the transmission flatjet.

Experimental Setup and Data Analysis. We used a recently reported transmission flatjet setup²³ at the undulator beamline UE52-SGM³³ of the BESSY II synchrotron radiation facility with similar experimental parameters as described before.¹⁴ Two colliding liquid jets were injected into vacuum using two nozzles with 48 μm inner diameter and at a sample flow rate between 3.0 and 3.2 ml/min, using a HPLC pump (Jasco PU-2085-Plus). The successively formed primary liquid sheet of the transmission flatjet was centered for normal incidence in the x-ray beam and was probed at effective thicknesses around 3 μm . The probed thickness was approximately constant in the range of the x-ray spot diameter of approximately 60 μm .³³ The liquid sample was trapped at liquid nitrogen temperature after probing. We used a monochromator slit size of 145 μm , corresponding to a spectral bandwidth of 300 meV at the Cr L-edge with a typical beamline flux on the order of 2×10^{12} photons/s (current of ~ 30 μA on a Hamamatsu G1127-04 2K photodiode, read out with a Keithley Electrometer model 6514B). For a spectrum scan of the Cr L-edge, the monochromator was scanned from 565 eV to 595 eV in steps of 0.1 eV with an integration time of 1 s per energy step. The duration of a single-scan was on the order of 10 min.

Spectra of the O K-edge were taken to determine the sample thickness (500 eV to 700 eV in steps of 2 eV). Transmission spectra were obtained from the ratio $T(h\nu)=I_T(h\nu)/I_0(h\nu)$ of flux transmitted through the sample $I_T(h\nu)$ with respect to the flux $I_0(h\nu)$, measured without the sample in the beam. The spectra were processed as discussed with Figs. S1-S5 of the Supporting Information (S.I.). The axis of incident photon energy is based on the calibration of the undulator beamline and agrees with the one in ref.¹³, as can be seen in the agreement of the L_3 -edge absorption maximum of $\text{Cr}^{\text{III}}(\text{acac})_3$ with that of $[\text{Cr}^{\text{III}}(\text{H}_2\text{O})_6]^{3+}$ in solution within less than 50 meV.

The employed sample thicknesses between 3.1 μm and 3.2 μm were determined separately for each Cr spectrum scan. These values are close to the thicknesses of around 3 μm used in our previous investigation¹⁴ and they are close to the theoretical optimum of 2.2 μm (estimated here for $h\nu=580$ eV in the same way as in ref.¹⁴).

The sample thicknesses were obtained from least-squares fits of the experimental transmission curves of ethanol with transmission data calculated using Beer-Lambert's law $T(h\nu)=\exp(-L/\Lambda(h\nu))$, where L is the sample thickness and $\Lambda(h\nu)$ is the experimental attenuation length of ethanol as detailed in Figs. S2-S4 in the S.I.. We note that reference spectra (I_0) were taken at the beginning and at the end of each experimental 12 hour shift here to guarantee accurate determination of I_0 and elimination of any experimental differences that may alter I_0 from day to day (from shift to shift). Fits of the measured $T(h\nu)$ with tabulated values were applied to data points in non-resonant spectral regions, namely between 500 and 530 eV, between 560 and 573 eV and between 591 and 700 eV for the O K-edge and between 560 and 573 eV for spectra at the Cr L-edge. We note that we fitted only the spectral region below the absorption onset of the Cr L-edge. In contrast to our preceding work in ref.¹⁴ this conceptually allows us to keep the information

on the absorption edge-jump on the high-energy side of the Cr L-edge as is discussed in the section III.

Sources for Experimental Uncertainties. The experimental spectra are affected by a number of sources of experimental noise and uncertainties. We here briefly outline how these uncertainties affect the average spectrum discussed in the following sections. First, source and readout noise: As discussed in our preceding publication,¹⁴ single-scan spectra are affected by a relative noise of minimally 0.1% in transmission due to the readout noise of our photodiode and potential instabilities of the x-ray source. Second, jet fluctuations on short time scales: Temporal fluctuations of the jet thickness, occurring on time scales on the order of 1 second and less, increase the noise of the diode current measured between two consecutive data points in a single-scan to the order of 0.2%-0.3% in transmission. These first and second noise contributions appear also in the averaged spectrum, with amplitudes decreasing for increasing numbers of averaged spectra. Both noise sources affect the statistical uncertainty of the absorption cross section determined for each data point in the averaged spectrum. Third, jet fluctuations on long time scales: Slow drifts of the jet thickness on time scales of around 1 min are observed during the acquisition time of a single-scan. For the way in which for Cr L-edge XAS we derive absorption spectra from the transmission spectra (including the edge-jump), these drifts show up as systematic errors in the absorption background of single-scan spectra. However, upon averaging over a number of spectra with different absorption backgrounds, we use their statistical variation to estimate the statistical uncertainty of absorption cross sections in the average spectrum. This uncertainty affects directly that of the absorption edge-jump, of integrated absorption cross sections and of the $L_3:L_2$ branching ratio. It can be reduced by improving the operation stability of the transmission flatjet.

CFM and CTM Multiplet Theory. Semi-empirical crystal field multiplet (CFM)³⁴ and charge transfer multiplet (CTM)³² calculations of ionic Cr³⁺ were performed in octahedral (O_h) symmetry for a ligand field splitting (10 Dq) of 2.1 eV, using the CTM4XAS interface (software release 5.5).³⁵ In CTM, a charge-transfer configuration 2p⁶3dⁿ⁺¹ \underline{L} was added to the 2p⁶3dⁿ ground state from CFM (where \underline{L} denotes a ligand hole) and charge transfer (CT) configurations 2p⁵3dⁿ⁺² \underline{L} were added to the 2p⁵3dⁿ⁺¹ core-excited final states. These additional configurations are known to produce satellite features on the high-energy sides of the L₃ and L₂ edges, respectively.³ Here the CTM spectrum of Cr³⁺ in O_h symmetry was calculated for 10 Dq=2.1 eV, Δ=1 eV, Q-U=1 eV and mixing parameters T_{eg}=0.5, T_{12g}=0.25. The choice of CFM and CTM parameters is based on the qualitative agreement of calculated and measured spectra (see discussion in the results section and Figs. S6 and S7 in the S.I. for comparison). All CFM and CTM spectra were shifted by the same offset in energy in order to best match with experiment in the L₃-edge maximum positions, unless further noticed. For all CFM and CTM calculations the Slater integrals were reduced to 80% of their Hartree-Fock atomic values (input values ‘1.0’ in the CTM4XAS interface). Recent findings by Hunault et al. show that non-equal scaling of F²_{dd} and F⁴_{dd} Slater integrals can lead to improved spectrum fits for the CFM model,³⁶ however, such investigations are beyond the scope of our conceptual study. All CFM and CTM spectra were calculated for T=300 K with Lorentzian lifetime broadenings of 0.2 eV and 0.6 eV (FWHM) for the L₃ and L₂ edges, respectively,³⁷ and a Gaussian broadening of 0.3 eV (FWHM), reflecting the incident energy bandwidth.

Restricted Active Space (RAS) Calculations. Ab initio restricted active space (RAS) calculations^{17, 38-39} were used to simulate L-edge XAS spectra of Cr^{III}(acac)₃. As in our preceding work we reduced the computational cost by performing the RAS calculations on a truncated molecular structure where six terminal methyl groups were replaced by hydrogen atoms with

negligible effects on the spectrum.^{11, 14} The Cr-O bond lengths obtained from DFT/B3LYP solvent optimization are between 1.977 and 1.978 Å for the full complex and between 1.972 and 1.973 Å for the truncated complex used for the RAS calculation. This is consistent with crystallographic investigations that report bond lengths between 1.95 and 1.97 Å.²⁵⁻²⁶ Spectrum calculations were performed with MOLCAS 7.9⁴⁰ at the RASPT2/ANO-RCC-VDZP level,⁴¹ using the polarized continuum model (PCM) for the ethanol solvent. The use of the computationally less demanding VDZP-level basis set is supported by the nearly identical L-edge XAS spectra obtained with VDZP and VTZP-level calculations for manganese acetylacetonates.^{11, 14} In the RAS calculations, a minimal active space consisting of the five metal-3d dominated orbitals were placed in the RAS2 space. The Cr 2p orbitals were placed in the RAS3 space, allowing a maximum of five electrons (at least one hole) in the core excited states. All possible configurations that represent single core excitations were included. To ensure that the hole stays in the Cr 2p orbitals (instead of moving to orbitals with higher energy), these orbitals were frozen in the RASSCF optimizations. RASPT2 calculations were performed using the default ionization potential electron affinity (IPEA) shift of 0.25 Hartree and an imaginary shift of 0.1 Hartree. The sensitivity of the RAS results to different model choices is shown in detail in ref.⁴² The oscillator strengths (absorption strengths) were calculated between orthogonal states formed from a RAS state-interaction approach that also includes spin-orbit coupling.⁴³ The spectra were calculated for T=300 K with Lorentzian life-time broadenings of 0.2 eV and 0.6 eV (FWHM) for the L₃ and L₂ edges, respectively,³⁷ and a Gaussian broadening of 0.3 eV (FWHM), reflecting the incident energy bandwidth. All spectra calculated with RAS were shifted by -2.54 eV to match the calculated with the experimental L₃-edge absorption maximum.

III. Results and Discussion

L-edge Transmission XAS of Cr^{III}(acac)₃ in Solution. We show in Fig. 2A superimposed single-scan transmission spectra of ethanol and of a dilute Cr^{III}(acac)₃ solution in ethanol (20 mM) including the spectral ranges of the O K-edge and the Cr L-edge. The figure illustrates that the Cr L-edge around 580 eV is very close to the near-edge absorption resonances of the O K-edge at 540 eV merging at higher energies with the O K-edge extended x-ray absorption fine structure (EXAFS) at 580 eV and beyond⁴⁴⁻⁴⁶. Therefore, even more than for Mn L-edge XAS¹⁴ or Fe L-edge XAS²⁴ careful treatment of the absorption background due to the solvent and its changes due to possible instabilities of the flatjet thickness is necessary for Cr L-edge XAS (see methods section and Figs. S2-S4 in the S.I. for a more detailed discussion of this aspect).

Fig. 2B is a zoom into the Cr L-edge region of Fig. 2A and shows a typical single-scan transmission spectrum of the Cr^{III}(acac)₃ solution sample. We observe two sets of resonant absorption dips in the transmission signal at the Cr L₃- and L₂-edges at around 578 eV and 586 eV, respectively (their splitting of 8.5 eV is due to spin-orbit interaction in the final core-excited states in the presence of the 2p core hole⁴). This is consistent with our preceding Mn L-edge XAS study with the transmission flatjet where we have shown that despite the strong O K-edge absorption of the solvent the method allows for detecting L-edge XAS of dilute metal solutes with concentrations ranging from 100s to 10s of mM.¹⁴

Absolute Absorption Cross Sections at the L-edge of Cr^{III}(acac)₃. In Fig. 3 we show the L-edge absorption spectrum of Cr^{III}(acac)₃ in solution, measured in absolute units of Mb (1 Mb=10⁻²² m²). This spectrum was obtained from averaging six single-scan spectra (total integration time of 1 hour) where the fitted solvent absorption (see methods section) was subtracted from each of

the scans separately (for the full spectrum range, see Fig. S5A in the S.I.). In Fig. 3A we maintain information on the absorption edge-jump on the high-energy side of the Cr L₂-edge at 590 eV and above due to the 2p ionization continuum. In electron yield-detected L-edge XAS this edge-jump is used, for example, for spectrum normalization³. In our data the amplitude of this edge-jump is affected by a large uncertainty on the order of 100% (1 σ statistical uncertainty).

For comparison, we overlay our spectrum with the experimental L-edge XAS spectrum of solid Cr^{III}(acac)₃ published by Carlotto et al.⁴⁷ (for easier comparison this spectrum was shifted by +6.4 eV and normalized to an absorption maximum of 8.9 Mb to align the reference spectrum with our spectrum). While the magnitudes of the absorption edge-jumps are comparable in the two spectra we note differences below and above the L₃- and L₂-edges. Using the energy alignment of the two spectra as in Fig. 3, in the solid-state spectrum intensities seem to be redistributed from below to above the edge maxima. This could be an indication of dose-dependent x-ray induced sample damage characteristic for x-ray absorption studies of high-valent transition metal complexes with synchrotron radiation, occurring at absorbed doses on the order of 10⁶ Gy (1 Gy=1 J/kg).¹⁵⁻¹⁶ Within our approach, using a fast flowing liquid flatjet, we measure x-ray absorption spectra with average doses around 60 Gy, which guarantees spectrum measurements free from sample-damage. We found no indications for the x-ray dose absorbed by the sample in ref.⁴⁷.

As current theoretical approaches do not take into account the absorption edge-jump we omit this information in the following and keep the spectrum in Fig. 3A for potential discussions in the future. For the spectrum shown in Fig. 3B, we subtracted a fitted linear background from each single-scan before averaging (see Fig. S5B in the S.I.). The L₃-edge of Cr^{III}(acac)₃ in Fig. 3B has a relatively sharp absorption peak at 578.2 eV. The absorption cross section peaks at 8.9 \pm 1.4 Mb (1 σ statistical uncertainty). This cross section is on the same order of magnitude as the L-edge

absorption cross sections of 12.4 Mb and 8.8 Mb for $\text{Mn}^{\text{II}}(\text{acac})_2$ and $\text{Mn}^{\text{III}}(\text{acac})_3$, respectively.¹⁴ We observe a clear “pre-edge” peak around 1.5 eV below the main peak and a weak shoulder around 2.5 eV below the main peak. The high-energy side of the L_3 -edge appears with a smooth slope. The L_2 -edge features are less distinct, which is consistent with the larger lifetime broadening in the L_2 than the L_3 -edge.³⁷

Our L-edge XAS spectrum of $\text{Cr}^{\text{III}}(\text{acac})_3$ is similar to the spectrum of $[\text{Cr}^{\text{III}}(\text{H}_2\text{O})_6]^{3+}$ in aqueous solution.¹³ Both complexes have octahedral coordination environments with similar ligand field splittings $10 Dq$ on the order of 2.2 eV²⁷⁻²⁹ for $\text{Cr}^{\text{III}}(\text{acac})_3$ and 2 eV¹³ for $[\text{Cr}^{\text{III}}(\text{H}_2\text{O})_6]^{3+}$.²⁷⁻²⁹ This is consistent with the closely situated H_2O and $(\text{acac})^-$ ligand species in the spectrochemical series.⁴⁸ Similar ligand-field splittings and L-edge XAS spectra have also been reported for Cr^{III} oxides.⁵ These similarities may be explained by the ionic character of the $\text{Cr}^{\text{III}}(\text{acac})_3$ complex and the predominance of atomic multiplet effects in the L-edge spectra.

CFM and CTM Calculations. In Fig. 4 we now compare the experimental spectrum of $\text{Cr}^{\text{III}}(\text{acac})_3$ to simulated spectra from the CFM approach, using $10 Dq=2.1$ eV (cf. Fig. S6 in the S.I.), and to spectra calculated with the CTM and RAS approaches. The ligand-field splitting of 2.1 eV is a reasonable choice, close to the ligand-field splittings of 2.21-2.24 eV from UV-vis spectroscopy,²⁷⁻²⁹ while at the same time giving a decent match to experiment. (For $\text{Mn}^{\text{III}}(\text{acac})_3$ we found a smaller $10 Dq$ in the CFM model (1.5 eV) than reported from UV-vis spectroscopy (around 2.2 eV) and tentatively assigned this to a reduction of $10 Dq$ due to core-hole effects.)¹⁴ The CTM spectrum (middle row in Fig. 4) is based on the same parameters as the CFM spectrum but, in addition, includes charge transfer (CT) states in the initial ground state ($2p^6 3d^{n+1} \underline{L}$ added to $2p^6 3d^n$, where \underline{L} denotes a ligand hole) and the final core-excited states ($2p^5 3d^{n+2} \underline{L}$ added to $2p^5 3d^{n+1}$). For a detailed list of CFM and CTM parameters see the methods section, variations of

CTM parameters are shown in Fig. S7 in the S.I.. Comparison of CTM and CFM spectra in Fig. 4 reveals that the distinct pre-edge peak in the L_3 -edge, overpronounced in CFM, is weaker (and more broadly distributed) in the CTM calculation and the high-energy side of the L_3 and L_2 -edges in CTM have smoother slopes, in better agreement with experiment. The latter is consistent with observations made for Fe L-edge XAS, where CT states show spectral signatures in particular in the high-energy sides of the $L_{3,2}$ -edges.³

RAS Calculations. RAS modeling of ground and valence excited states of $\text{Cr}^{\text{III}}(\text{acac})_3$ gives a ligand-field splitting of 2.2 eV, the same value as in the UV/Vis experiments.²⁷⁻²⁹ The Cr L-edge XAS spectrum using the RAS approach is shown in Fig. 4 and there is good overall agreement with experiment. Similar to the CTM calculation the smooth slope on the high-energy side of the L_3 -edge is better described by RAS than by the CFM calculation. Similar to the CFM calculation the RAS spectrum, however, deviates from experiment in terms of the overpronounced pre-edge feature in the L_3 -edge and in the too strong main peak in the L_2 -edge. In contrast to the CTM spectrum and similar to the CFM spectrum, features appear to be too sharp in the RAS spectrum and this may point to limitations of the RAS calculations when using only five metal 3d-derived orbitals in the active space.^{11, 14, 17}

RAS allows for the decomposition of x-ray absorption spectra for the properties of the core-excited final states^{11, 17, 20} and we use this in Fig. 5A to analyze the $\text{Cr}^{\text{III}}(\text{acac})_3$ L-edge XAS spectrum for the differential orbital occupation numbers of t_{2g} and e_g orbitals in the core-excited final states as compared to the $t_{2g}^3 e_g^0$ ground state. For low incident energies, the final states roughly correspond to a $2p^5 t_{2g}^3 e_g^1$ (yellow e_g component in Fig. 5A): Upon 2p-3d core-excitation an electron is added to one of the unoccupied e_g -type orbitals resulting in the lowest electron configurations of a high-spin $3d^4$ system. At higher incident energies, the different configurations

mix strongly as indicated by the deviation of the e_g component in Fig. 5A from the cross section (black sum in Fig. 5A). In the limit of complete mixing, there is equal occupation of all five metal 3d-derived orbitals in the core-excited states, giving average population numbers of 0.8. This translates to negative contributions for the t_{2g} orbitals (green t_{2g} component in Fig. 5A) and larger than unity e_g contributions. This picture of strong mixing in the L-edge XAS spectrum of 3d transition metal systems with weak ligand fields aligns with previous observations for the Mn-acac complexes.¹⁰ Here the mixed configurations only matter at absorption energies higher than 577 eV and thus about 2 eV above the absorption onset of the spectrum, similar to the ligand field splitting of $\text{Cr}^{\text{III}}(\text{acac})_3$. In the present analysis, the orbital contributions for the low-energy sides of L_2 and L_3 edges differ. This is possibly an artifact from the perturbative treatment of spin-orbit coupling that overestimates the contribution from high-energy states with L_3 -type spin-orbit coupling in the L_2 -edge.

In Fig. 5B we show a decomposition of the RAS spectrum from Fig. 4 into contributions of different spin multiplicities in the core-excited final states. While the high-spin $\text{Cr}^{\text{III}}(\text{acac})_3$ complex in the ground state has three unpaired 3d-electrons with a total spin of $S=3/2$ and hence a spin multiplicity $(2S+1)$ of 4 (quartet), the core-excited final states are mixed from spin multiplicities of 2 (doublet), 4 (quartet) and 6 (sextet). The predominant intensity in the L_3 -edge maximum originates from quartet final states, consistent with the dominant $\Delta S=0$ components in the Mn L-edge XAS spectra of $\text{Mn}^{\text{II}}(\text{acac})_2$ and $\text{Mn}^{\text{III}}(\text{acac})_3$.¹¹ The spectrally weighted absorption energies of the different multiplicity components increase with decreasing spin multiplicity as found for $\text{Mn}^{\text{II}}(\text{acac})_2$ and $\text{Mn}^{\text{III}}(\text{acac})_3$ and this is consistent with a loss of favorable exchange interactions for lower spin multiplicities.¹¹ Similar decomposition analyses can also be performed within the DFT/ROCIS²² approach, as done by Carlotto et al. for $\text{Cr}^{\text{III}}(\text{acac})_3$.^{17, 47} In agreement

with our results from RAS, Carlotto et al. identified a predominant $\Delta S=0$ quartet component with DFT/ROCIS. However, the order of the spectral weight of sextet, quartet and doublet final states along the axis of incident photon energy differs from our RAS results. This different ordering of multiplicity components in the DFT/ROCIS calculations further highlights the differences between the DFT/ROCIS and RAS calculations.

L-edge Branching Ratios. The statistical branching ratio $I(L_3)/I(L_2+L_3)$ is $2/3$, calculated from the number of degenerate states in the L_3 ($j=3/2$, 4 states) and L_2 ($j=1/2$, 2 states) edges. However, this ratio only holds in the absence of both spin orbit coupling in the initial-state and electrostatic interactions between core-hole and valence electrons in the final states. In real complexes, spin-orbit coupling and electrostatic interactions lead to significant changes in the branching ratios, which can be used to get signatures of the d-electron counts and the spin multiplicities.¹² We determine for the $\text{Cr}^{\text{III}}(\text{acac})_3$ spectrum a branching ratio of $I(L_3)/I(L_2+L_3)=0.47\pm 0.10$ (1σ statistical uncertainty), where we used an arbitrary cutoff energy of 582 eV to distinguish L_3 - and the L_2 -edges (variation of this cutoff energy within reasonable limits of ± 1 eV does not change the branching ratio to beyond the experimental uncertainty limits). We checked that linear background subtraction (as applied here) as compared to subtraction of $L_{3,2}$ -edge edge-jumps as applied, for example, in ref.³ does not alter the branching ratio beyond the experimental uncertainty limits. We note that the branching ratio of $\text{Cr}^{\text{III}}(\text{acac})_3$ ($3d^3$, $S=3/2$) is around 30% smaller than the branching ratio of 0.66 ± 0.02 reported earlier for $\text{Mn}^{\text{III}}(\text{acac})_3$ ($3d^4$, $S=2$) and around 35% smaller than the branching ratio of 0.72 ± 0.02 reported for of $\text{Mn}^{\text{II}}(\text{acac})_2$ ($3d^5$, $S=5/2$) as shown in Fig. 6 (the larger uncertainty for $\text{Cr}^{\text{III}}(\text{acac})_3$ as compared to the Mn complexes is due to the lower concentration and a less stable operation of the flatjet for this sample)¹⁴ This demonstrates that the L-edge XAS branching ratio is potentially useful to

distinguish between two neighboring oxidation states, or alternatively, two different spin states of the same complex.

A stronger connection between branching ratios and the 3d spin configuration can be made through the use of a theoretical model. The calculated spectra from CFM and CTM (as shown in Fig. 4) have branching ratios between 0.55 and 0.56, which are within the error bars of the experiment. They are consistent with the branching ratio of 0.58 calculated by Thole et al. for ionic Cr^{3+} (where a typical reduction factor 0.75 was applied to all Slater integrals).¹² For $\text{Cr}^{\text{III}}(\text{acac})_3$ RAS gives a similar branching ratio of 0.56, again within the error bars as shown in Fig. 6. Good agreement was found earlier for $\text{Mn}^{\text{III}}(\text{acac})_3$, while for $\text{Mn}^{\text{II}}(\text{acac})_2$ the branching ratio was overestimated in the RAS calculations.¹⁴ The trend of increasing branching ratio as a function of increasing nominal 3d occupation and spin multiplicity is reproduced in the RAS calculations (from 0.56 to 0.65 to 0.78). This trend is also expected from multiplet calculations for ionic systems.¹² However, the deviations between RAS and experimental results are larger than the uncertainties in the experiment. This suggests that the calculations of the branching ratio in the RAS calculations can be improved. We have previously speculated that the deviations are due to perturbative treatment of the strong spin-orbit coupling,¹⁴ and it is possible that improved results would require at least a 2-component relativistic approach.⁴⁹⁻⁵¹

Integrated Absolute Absorption Cross Sections. In our preceding study we have outlined how the integrated absolute absorption cross sections, here named absorption integrals, of metal L-edge XAS spectra can be used to extract information on the occupation number or, alternatively, the number of “holes” in the metal 3d shell.¹⁴ Previous studies at the Fe L-edge have shown that comparison of integrated absorption spectra not only can provide information on the number of electrons in the metal 3d-derived orbitals but also on a more detailed level on their

covalent or, inversely, their metal ionic character.^{3, 6-7} However, while comparing absorption integrals for electron yield-detected XAS requires sensitive normalization schemes,³ transmission-detected XAS holds the promise to allow for directly determining absolute absorption cross sections.¹⁴ The absorption integral of the experimental $\text{Cr}^{\text{III}}(\text{acac})_3$ spectrum (Fig. 3B) amounts to $45 \pm 12 \text{ Mb} \cdot \text{eV}$, as integrated over the full L-edge between 573 and 590 eV. That of the L_3 -edge region is $21.7 \pm 8.7 \text{ Mb} \cdot \text{eV}$, as integrated between 573 and 582 eV (1σ statistical uncertainties). The experimental error bars are significantly larger than the systematic uncertainties due to different background subtraction scheme (linear background as applied here vs. edge-jump background as applied, for example, in ref.³).

In Fig. 7 we combine these values with our earlier results from $\text{Mn}^{\text{II}}(\text{acac})_2$ and $\text{Mn}^{\text{III}}(\text{acac})_3$. We compare the absorption integrals of $\text{Cr}^{\text{III}}(\text{acac})_3$ ($3d^3$, 7 holes) with $\text{Mn}^{\text{III}}(\text{acac})_3$ ($3d^4$, 6 holes) and $\text{Mn}^{\text{II}}(\text{acac})_2$ ($3d^5$, 5 holes) for the entire L-edge region (Fig. 7A) and for the L_3 -edge only (Fig. 7B) as a function of the nominal number of holes in the metal 3d orbitals or, alternatively, the nominal 3d occupation number. Assuming that the degree of covalency of the metal 3d-derived molecular orbitals is equal for these three predominantly ionic systems, one would expect a linear increase of absorption integrals where the integrated absorption cross section is proportional to the nominal number of 3d holes (proportional to 10 minus the nominal 3d occupation). Reflecting this simple expectation we included in Figs. 7A and 8B fits to the data using uncertainty-weighted least-squares fits where the lines cross the origins in the plots (“no absorption without 3d holes”). This linear fit may approximate the experimental absorption integrals of the entire L-edge reasonably well within the error bars (Fig. 7A) although it has to be noted that an improved signal to noise ratio will be necessary in future experiments to conclusively claim this. The linear fit certainly, and this can be stated with the experimental error bars given here, fails to describe the

integrals of the L₃-edges only (Fig. 7B). This deviation is consistent with the trend observed in the branching ratios which decrease from Mn^{II}(acac)₂ to Mn^{III}(acac)₃ and to Cr^{III}(acac)₃ and thereby decrease the relative intensities of the L₃-edges with respect to the full L-edges along this series. Correlating only L₃-edge absorption integrals of different systems with their electronic structure and in particular their covalent character, therefore, does not seem favorable due to the effects affecting L₃ and L₂ intensities differently (spin-orbit coupling and electrostatic interactions).

In general, we note that the experimental error bars of absorption integrals in our data are comparably large due to statistical variations in the single-scan spectra. For the absorption integrals, the error bars (± 12 Mb·eV for Cr^{III}) are larger than the difference expected for two complexes differing by one 3d hole (≤ 3.8 Mb·eV, i.e. half of 7.6 Mb·eV, as estimated from the linear fit of our experimental data). To correlate absorption integrals with the number of 3d-holes and the covalent character of the metal 3d-derived orbitals would therefore require the error bars to be decreased by an order of magnitude. Future measurements with better knowledge of the flatjet thickness, e.g. by online monitoring, could allow for a more detailed comparison of absorption integrals between different complexes. Comparison of absorption integrals over the full L-edges could then be used for assessments of the ionic or covalent characters of the metal-ligand bonds. We note that determination of the branching ratio is less affected by fluctuations in the flatjet thickness because changes in the background partly cancel when comparing the intensities of the two edges.

As a further test of our calculations we compare in Figs. 7A and 8B the measured and calculated absorption integrals from RAS where the RAS data are given in units of oscillator strengths ('o.s.'). The axes of calculated and experimental absorption integrals in Fig. 7 are scaled such that the linear fits of the experimental and the RAS data coincide. This comparison shows

that the relative absorption integrals from RAS qualitatively reproduce an approximately linearly increasing absorption integral for the whole L-edge. For Mn^{II} the RAS estimate is slightly outside the experimental error bars. It is possible that this deviation is due to the use of only the metal 3d-dominated orbitals in the active space. Consistently with the correct description of the increasing branching ratio the RAS calculation also correctly describes the non-linear variation of the L_3 absorption integral with the number of 3d holes (Fig. 7B).

IV. Conclusion

We present the first Cr L-edge absorption spectrum of $\text{Cr}^{\text{III}}(\text{acac})_3$ in solution, measured in transmission and free from x-ray induced sample damage with a transmission flatjet. We provide absolute absorption cross sections with a peak value at the L_3 -edge of 8.9 ± 1.4 Mb and an integral value (integrated over the whole L-edge) of 45 ± 12 Mb·eV. In contrast to partial-fluorescence yield detected absorption, transmission spectra give spectral shapes and branching ratios unaffected by state-dependent fluorescence yield, which enables straightforward comparison to theoretical predictions of absorption intensities. With a combination of semi-empirical multiplet and restricted active space (RAS) calculations we assess the information content of the L-edge absorption spectrum with respect to the local electronic structure of the $\text{Cr}^{\text{III}}(\text{acac})_3$ complex. Similar to our findings for the $\text{Mn}^{\text{III}}(\text{acac})_3$ complex, we discuss the pre-edge peak in the L_3 -edge in relation to the presence of an octahedral ligand field splitting and find that a value of around 2 eV is consistent with results from UV-vis investigations. Charge transfer states are reflected in a smooth slope at the high-energy side of the L_3 -edge. Orbital and spin analyses of core-excited final states with RAS show that the L-edge absorption spectrum of $\text{Cr}^{\text{III}}(\text{acac})_3$ is affected by strong mixing of configurations in the final core-excited states.

We find that the branching ratio of $\text{Cr}^{\text{III}}(\text{acac})_3$ with a nominal 3d-occupation of 3 is significantly smaller than that of $\text{Mn}^{\text{II}}(\text{acac})_2$ and $\text{Mn}^{\text{III}}(\text{acac})_3$ with 3d-occupations of 5 and 4, respectively. This experimental observation is consistent with the results from multiplet and RAS calculations. The uncertainties in experimental branching ratios are smaller than the difference between the complexes, making this a reliable fingerprint of spin multiplicity in this $\text{Cr}^{\text{III}}(\text{d}^3)$ - $\text{Mn}^{\text{III}}(\text{d}^4)$ - $\text{Mn}^{\text{II}}(\text{d}^5)$ series. Deviations between experiment and calculations point to possible improvements in the RAS perturbative description of spin-orbit coupling. The absorption cross sections integrated over the whole L-edge are consistent with a linear increase of absorption integrals with decreasing 3d occupation (increasing number of nominal 3d holes). This trend is reproduced by the RAS calculations. The integrated absorption cross sections of only the L_3 -edge, however, markedly deviate from this linear relationship which is consistent with differences in the respective L-edge branching ratios. From our data we estimate that for being able to assess details of this relationship and the covalent character of the metal-ligand bonds in particular, a decrease in experimental uncertainties by an order of magnitude would be required.

Supporting Information

Details on the data analysis; multiplet calculations.

Acknowledgments

We gratefully acknowledge the continuous support by the BESSY II staff and we thank HZB for the allocation of synchrotron radiation beamtime. We acknowledge financial support from the Human Frontiers Science Program (RGP0063/2013), the Swedish Research Council, and the Knut and Alice Wallenberg Foundation (Grant No. KAW-2013.0020). The computations were performed on resources provided by SNIC through Uppsala Multidisciplinary Center for Advanced Computational Science (UPPMAX) under project snic2016-1-464 and National Supercomputer Centre at Linköping University (Triolith) under project snic2016-1-508. We acknowledge funding from the German Science Foundation (Project No. DFG-NI 492/11-1). Parts of this research is supported by the Director, Office of Science, Office of Basic Energy Sciences, Division of Chemical Sciences, Geosciences, and Biosciences of the Department of Energy under contract DE-AC02-05CH11231 (J.Y., V.K.Y.), and by the NIH Grants GM110501 (J.Y.), GM126289 (J.K.) and GM55302 (V.K.Y.).

Author Contributions

Conceived the experiment: M.K., Ph.W.

Designed the experiment: M. K., M.E., J.K., V.K.Y., J.Y., E.T.J.N., Ph.W.

Prepared the samples: M.K., M.E.

Carried out the experiment: M.K., M.E.

Analyzed the data: M.K. under the supervision of Ph.W.

Carried out ab-initio restricted active space calculations: M.G., E. K., M.L.

Carried out multiplet calculations: M.K.

Wrote the paper: M.K., with contributions from all authors.

References

1. Cramer, S. P.; DeGroot, F. M. F.; Ma, Y.; Chen, C. T.; Sette, F.; Kipke, C. A.; Eichhorn, D. M.; Chan, M. K.; Armstrong, W. H., Ligand field strengths and oxidation states from manganese L-edge spectroscopy. *Journal of the American Chemical Society* **1991**, *113* (21), 7937-7940.
2. De Groot, F. M. F.; Fuggle, J. C.; Thole, B. T.; Sawatzky, G. A., 2p x-ray absorption of 3d transition-metal compounds: An atomic multiplet description including the crystal field. *Physical Review B* **1990**, *42* (9), 5459-5468.
3. Wasinger, E. C.; de Groot, F. M. F.; Hedman, B.; Hodgson, K. O.; Solomon, E. I., L-edge x-ray absorption spectroscopy of non-heme iron sites: experimental determination of differential orbital covalency. *Journal of the American Chemical Society* **2003**, *125* (42), 12894-12906.
4. Van der Laan, G.; Kirkman, I., The 2p absorption spectra of 3d transition metal compounds in tetrahedral and octahedral symmetry. *Journal of Physics: Condensed Matter* **1992**, *4* (16), 4189.
5. Theil, C.; van Elp, J.; Folkmann, F., Ligand field parameters obtained from and chemical shifts observed at the Cr $L_{2,3}$ edges. *Physical Review B* **1999**, *59* (12), 7931-7936.
6. Hocking, R. K.; Wasinger, E. C.; De Groot, F. M. F.; Hodgson, K. O.; Hedman, B.; Solomon, E. I., Fe L-edge XAS studies of $K_4[Fe(CN)_6]$ and $K_3[Fe(CN)_6]$: A direct probe of back-bonding. *Journal of the American Chemical Society* **2006**, *128* (32), 10442-10451.
7. Wilson, S. A.; Kroll, T.; Decreau, R. A.; Hocking, R. K.; Lundberg, M.; Hedman, B.; Hodgson, K. O.; Solomon, E. I., Iron L-edge X-ray absorption spectroscopy of oxy-picket fence porphyrin: experimental insight into Fe-O₂ bonding. *J Am Chem Soc* **2013**, *135* (3), 1124-36.
8. Kubin, M.; Kern, J.; Gul, S.; Kroll, T.; Chatterjee, R.; Löchel, H.; Fuller, F. D.; Sierra, R. G.; Quevedo, W.; Weniger, C., et al., Soft x-ray absorption spectroscopy of metalloproteins and high-valent metal-complexes at room temperature using free-electron lasers. *Structural Dynamics* **2017**, *4* (5), 054307.
9. Kunnus, K.; Zhang, W.; Delcey, M. G.; Pinjari, R. V.; Miedema, P. S.; Schreck, S.; Quevedo, W.; Schröder, H.; Föhlisch, A.; Gaffney, K. J., et al., Viewing the valence electronic structure of ferric and ferrous hexacyanide in solution from the Fe and cyanide perspectives. *The Journal of Physical Chemistry B* **2016**, *120* (29), 7182-7194.
10. Glatzel, P.; Bergmann, U.; Yano, J.; Visser, H.; Robblee, J. H.; Gu, W.; De Groot, F. M. F.; Christou, G.; Pecoraro, V. L.; Cramer, S. P., et al., The electronic structure of Mn in oxides, coordination complexes, and the oxygen-evolving complex of photosystem II studied by resonant inelastic X-ray scattering. *Journal of the American Chemical Society* **2004**, *126* (32), 9946-9959.
11. Kubin, M.; Guo, M.; Kroll, T.; Löchel, H.; Källman, E.; Baker, M. L.; Mitzner, R.; Gul, S.; Kern, J.; Föhlisch, A., et al., Probing the oxidation state of transition metal complexes: A case study on how charge and spin densities determine Mn L-edge X-ray absorption energies. (*submitted*) **2018**.
12. Thole, B. T.; van der Laan, G., Branching ratio in x-ray absorption spectroscopy. *Physical Review B* **1988**, *38* (5), 3158-3171.
13. Wernet, P.; Kunnus, K.; Schreck, S.; Quevedo, W.; Kurian, R.; Techert, S.; de Groot, F. M.; Odelius, M.; Föhlisch, A., Dissecting local atomic and intermolecular interactions of transition-metal ions in solution with selective X-ray spectroscopy. *J Phys Chem Lett* **2012**, *3* (23), 3448-53.
14. Kubin, M.; Guo, M.; Ekimova, M.; Baker, M. L.; Kroll, T.; Källman, E.; Kern, J.; Yachandra, V. K.; Yano, J.; Nibbering, E. T. J., et al., Direct determination of absolute absorption cross sections at the L-edge of dilute Mn complexes in solution using a transmission flatjet. *Inorganic Chemistry* **2018**, *57* (9), 5449-5462.
15. Yano, J.; Kern, J.; Irrgang, K. D.; Latimer, M. J.; Bergmann, U.; Glatzel, P.; Pushkar, Y.; Biesiadka, J.; Loll, B.; Sauer, K., et al., X-ray damage to the Mn₄Ca complex in single crystals of photosystem II: a case study for metalloprotein crystallography. *Proc Natl Acad Sci U S A* **2005**, *102* (34), 12047-52.

16. van Schooneveld, M. M.; DeBeer, S., A close look at dose: Toward L-edge XAS spectral uniformity, dose quantification and prediction of metal ion photoreduction. *Journal of Electron Spectroscopy and Related Phenomena* **2015**, *198*, 31-56.
17. Pinjari, R. V.; Delcey, M. G.; Guo, M.; Odelius, M.; Lundberg, M., Restricted active space calculations of L-edge X-ray absorption spectra: from molecular orbitals to multiplet states. *J Chem Phys* **2014**, *141* (12), 124116.
18. Josefsson, I.; Kunnus, K.; Schreck, S.; Fohlich, A.; de Groot, F.; Wernet, P.; Odelius, M., Ab initio calculations of X-ray spectra: atomic multiplet and molecular orbital effects in a multiconfigurational SCF approach to the L-edge spectra of transition metal complexes. *J Phys Chem Lett* **2012**, *3* (23), 3565-70.
19. Preuße, M.; Bokarev, S. I.; Aziz, S. G.; Kühn, O., Towards an ab initio theory for metal L-edge soft X-ray spectroscopy of molecular aggregates. *Structural Dynamics* **2016**, *3* (6), 062601.
20. Bokarev, S. I.; Khan, M.; Abdel-Latif, M. K.; Xiao, J.; Hilal, R.; Aziz, S. G.; Aziz, E. F.; Kühn, O., Unraveling the electronic structure of photocatalytic manganese complexes by L-edge X-ray spectroscopy. *The Journal of Physical Chemistry C* **2015**, *119* (33), 19192-19200.
21. Thole, B. T.; Van Der Laan, G.; Fuggle, J. C.; Sawatzky, G. A.; Karnatak, R. C.; Esteve, J. M., 3d x-ray-absorption lines and the 3d⁹4fⁿ+1 multiplets of the lanthanides. *Physical Review B* **1985**, *32* (8), 5107-5118.
22. Roemelt, M.; Maganas, D.; DeBeer, S.; Neese, F., A combined DFT and restricted open-shell configuration interaction method including spin-orbit coupling: application to transition metal L-edge X-ray absorption spectroscopy. *J Chem Phys* **2013**, *138* (20), 204101.
23. Ekimova, M.; Quevedo, W.; Faubel, M.; Wernet, P.; Nibbering, E. T., A liquid flatjet system for solution phase soft-x-ray spectroscopy. *Struct Dyn* **2015**, *2* (5), 054301.
24. Fondell, M.; Eckert, S.; Jay, R. M.; Weniger, C.; Quevedo, W.; Niskanen, J.; Kennedy, B.; Sorgenfrei, F.; Schick, D.; Giangrisostomi, E., et al., Time-resolved soft X-ray absorption spectroscopy in transmission mode on liquids at MHz repetition rates. *Structural Dynamics* **2017**, *4* (5), 054902.
25. Kuroda, R.; Mason, S. F., Crystal structure and absolute configuration of (-)-tris(pentane-2,4-dionato)chromium(III). *Journal of the Chemical Society, Dalton Transactions* **1979**, (2), 273-278.
26. Morosin, B., The crystal structure of trisacetylacetonatochromium(III). *Acta Crystallographica* **1965**, *19* (1), 131-137.
27. Nordén, B., Circular dichroism spectrum and absolute configuration of tris(acetylacetonato)chromium(III). *Inorganic and Nuclear Chemistry Letters* **1975**, *11* (6), 387-394.
28. Drake, A. F.; Gould, J. M.; Mason, S. F.; Rosini, C.; Woodley, F. J., The optical resolution of tris(pentane-2,4-dionato)metal(III) complexes. *Polyhedron* **1983**, *2* (6), 537-538.
29. Piper, T. S.; Carlin, R. L., Crystal spectrum of chromium acetylacetonate and the ligand field in trigonal coordination compounds. *The Journal of Chemical Physics* **1962**, *36* (12), 3330-3332.
30. Kurian, R.; Kunnus, K.; Wernet, P.; Butorin, S. M.; Glatzel, P.; de Groot, F. M., Intrinsic deviations in fluorescence yield detected x-ray absorption spectroscopy: the case of the transition metal L(2),(3) edges. *J Phys Condens Matter* **2012**, *24* (45), 452201.
31. de Groot, F. M. F.; Arrio, M. A.; Sainctavit, P.; Cartier, C.; Chen, C. T., Fluorescence yield detection: Why it does not measure the X-ray absorption cross section. *Solid State Communications* **1994**, *92* (12), 991-995.
32. Groot, F. d., Multiplet effects in X-ray spectroscopy. *Coordination Chemistry Reviews* **2005**, *249* (1-2), 31-63.
33. Miedema, P. S.; Quevedo, W.; Fondell, M., The variable polarization undulator beamline UE52 SGM at BESSY II. *Journal of large-scale research facilities JLSRF* **2016**, *2*, 70.
34. de Groot, F. M. F.; Fuggle, J. C.; Thole, B. T.; Sawatzky, G. A., 2px-ray absorption of 3d transition-metal compounds: An atomic multiplet description including the crystal field. *Physical Review B* **1990**, *42* (9), 5459-5468.

35. Stavitski, E.; de Groot, F. M. F., The CTM4XAS program for EELS and XAS spectral shape analysis of transition metal L edges. *Micron* **2010**, *41* (7), 687-694.
36. Hunault, M. O. J. Y.; Harada, Y.; Miyawaki, J.; Wang, J.; Meijerink, A.; de Groot, F. M. F.; van Schooneveld, M. M., Direct observation of Cr³⁺ 3d states in ruby: Toward experimental mechanistic evidence of metal chemistry. *The Journal of Physical Chemistry A* **2018**, *122* (18), 4399-4413.
37. Ohno, M.; van Riessen, G. A., Hole-lifetime width: a comparison between theory and experiment. *Journal of Electron Spectroscopy and Related Phenomena* **2003**, *128* (1), 1-31.
38. Guo, M.; Kallman, E.; Sorensen, L. K.; Delcey, M. G.; Pinjari, R. V.; Lundberg, M., Molecular orbital simulations of metal 1s2p resonant inelastic X-ray scattering. *J Phys Chem A* **2016**, *120* (29), 5848-55.
39. Guo, M.; Sorensen, L. K.; Delcey, M. G.; Pinjari, R. V.; Lundberg, M., Simulations of iron K pre-edge X-ray absorption spectra using the restricted active space method. *Phys Chem Chem Phys* **2016**, *18* (4), 3250-9.
40. Aquilante, F.; De Vico, L.; Ferre, N.; Ghigo, G.; Malmqvist, P. A.; Neogrady, P.; Pedersen, T. B.; Pitonak, M.; Reiher, M.; Roos, B. O., et al., MOLCAS 7: the next generation. *J Comput Chem* **2010**, *31* (1), 224-47.
41. Malmqvist, P. Å.; Pierloot, K.; Shahi, A. R. M.; Cramer, C. J.; Gagliardi, L., The restricted active space followed by second-order perturbation theory method: Theory and application to the study of CuO₂ and Cu₂O₂ systems. *Journal of Chemical Physics* **2008**, *128* (20).
42. Pinjari, R. V.; Delcey, M. G.; Guo, M.; Odelius, M.; Lundberg, M., Cost and sensitivity of restricted active-space calculations of metal L-edge X-ray absorption spectra. *Journal of Computational Chemistry* **2016**, *37* (5), 477-486.
43. Malmqvist, P. Å.; Roos, B. O.; Schimmelpfennig, B., The restricted active space (RAS) state interaction approach with spin-orbit coupling. *Chemical Physics Letters* **2002**, *357* (3-4), 230-240.
44. Teo, B.; Joy, D., *EXAFS spectroscopy: Techniques and Applications*. Springer: New York, 1981.
45. Bergmann, U.; Di Cicco, A.; Wernet, P.; Principi, E.; Glatzel, P.; Nilsson, A., Nearest-neighbor oxygen distances in liquid water and ice observed by x-ray Raman based extended x-ray absorption fine structure. *The Journal of Chemical Physics* **2007**, *127* (17), 174504.
46. Meibohm, J.; Schreck, S.; Wernet, P., Temperature dependent soft x-ray absorption spectroscopy of liquids. *Review of Scientific Instruments* **2014**, *85* (10), 103102.
47. Carlotto, S.; Floreano, L.; Cossaro, A.; Dominguez, M.; Rancan, M.; Sambri, M.; Casarin, M., The electronic properties of three popular high spin complexes [TM(acac)₃, TM = Cr, Mn, and Fe] revisited: an experimental and theoretical study. *Physical Chemistry Chemical Physics* **2017**, *19* (36), 24840-24854.
48. Shimura, Y.; Tsuchida, R., Absorption spectra of Co(III) complexes. II. Redetermination of the spectrochemical series. *Bulletin of the Chemical Society of Japan* **1956**, *29* (3), 311-316.
49. Fronzoni, G.; Stener, M.; Decleva, P.; Wang, F.; Ziegler, T.; van Lenthe, E.; Baerends, E. J., Spin-orbit relativistic time dependent density functional theory calculations for the description of core electron excitations: TiCl₄ case study. *Chemical Physics Letters* **2005**, *416* (1), 56-63.
50. Casarin, M.; Finetti, P.; Vittadini, A.; Wang, F.; Ziegler, T., Spin-orbit relativistic time-dependent density functional calculations of the metal and ligand pre-edge XAS intensities of organotitanium complexes: TiCl₄, Ti(η⁵-C₅H₅)Cl₃, and Ti(η⁵-C₅H₅)₂Cl₂. *The Journal of Physical Chemistry A* **2007**, *111* (24), 5270-5279.
51. Bunău, O.; Joly, Y., Full potential x-ray absorption calculations using time dependent density functional theory. *Journal of Physics: Condensed Matter* **2012**, *24* (21), 215502.

Figures

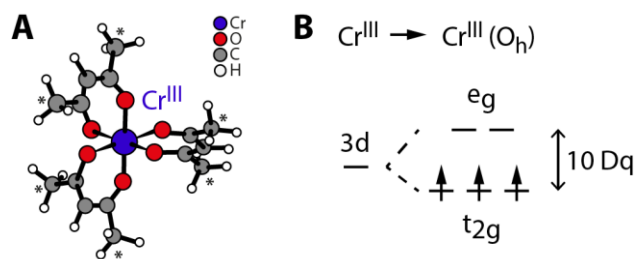


Figure 1. Molecular (A) and valence electronic structure (B) of $\text{Cr}^{\text{III}}(\text{acac})_3$. The cartoon shown in (A) is based on the structure optimized with density functional theory. Terminal methyl groups marked with * in (A) were replaced by hydrogen atoms for the restricted active space (RAS) calculations. (B) Cr 3d orbitals with nominal $3d^3$ occupation, split into three t_{2g} and two e_g orbitals.

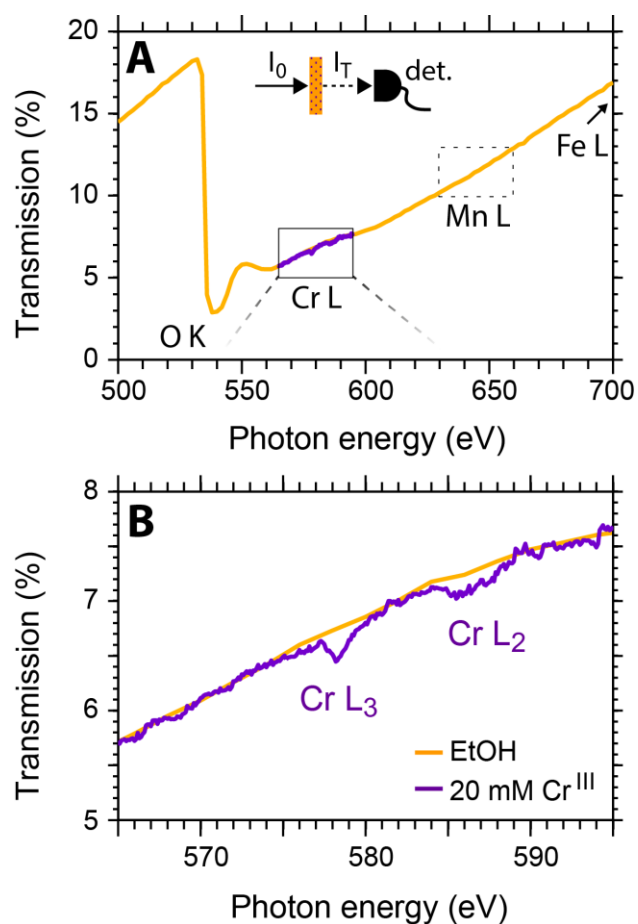


Figure 2. (A) Raw transmission spectrum of 20 mM Cr^{III}(acac)₃ solution in ethanol (purple, single-scan) and spectrum of the ethanol solvent (orange), as measured with the transmission flatjet in a spectral region relevant to Cr L-edge x-ray absorption spectroscopy in solution. The Cr L-edge region overlaps with O K-edge near-edge and extended x-ray absorption fine structure (EXAFS) features of the solvent. Inset: probing scheme for transmission-detected x-ray absorption spectroscopy. (B) Magnification of the Cr L-edge region from (A). For better inspection, the Cr L-edge data as measured with a flatjet thickness of 3.19 μm was rescaled to the O K-edge data measured at a thickness of 3.15 μm .

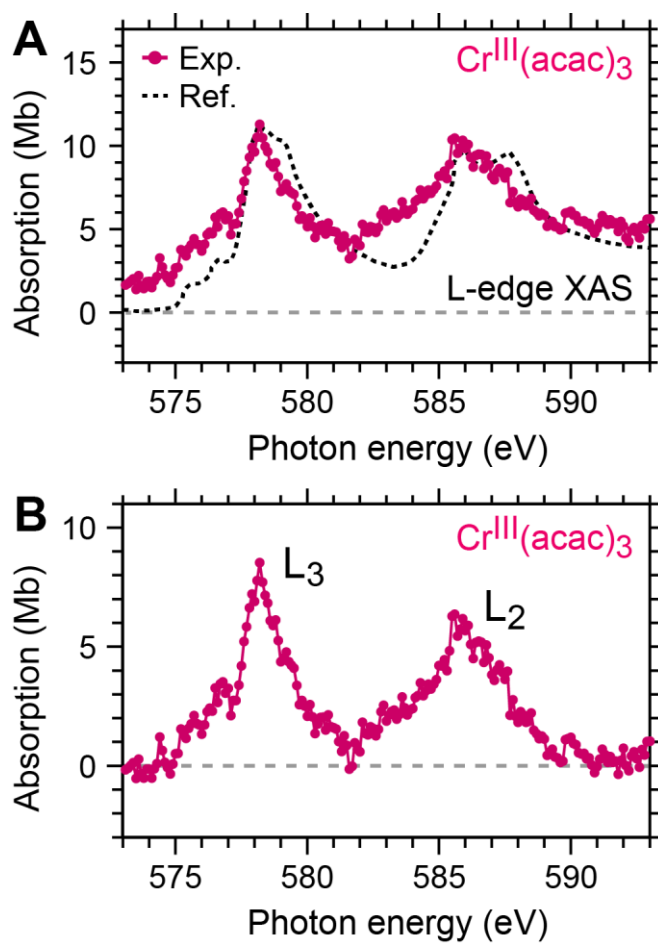


Figure 3. Experimental Cr L-edge x-ray absorption spectrum of $\text{Cr}^{\text{III}}(\text{acac})_3$ in solution where absolute absorption cross sections are determined from the transmission measurements and are shown in units of Mb ($1 \text{ Mb} = 10^{-28} \text{ m}^2$). The average spectrum is shown (A) without and (B) with subtraction of a fitted linear background from each individual scan before averaging six single-scans. The spectrum in (A) is overlaid with the spectrum of solid $\text{Cr}^{\text{III}}(\text{acac})_3$, published in ref. 47, shifted by +6.4 eV and normalized to the maximum intensity of our experimental spectrum.

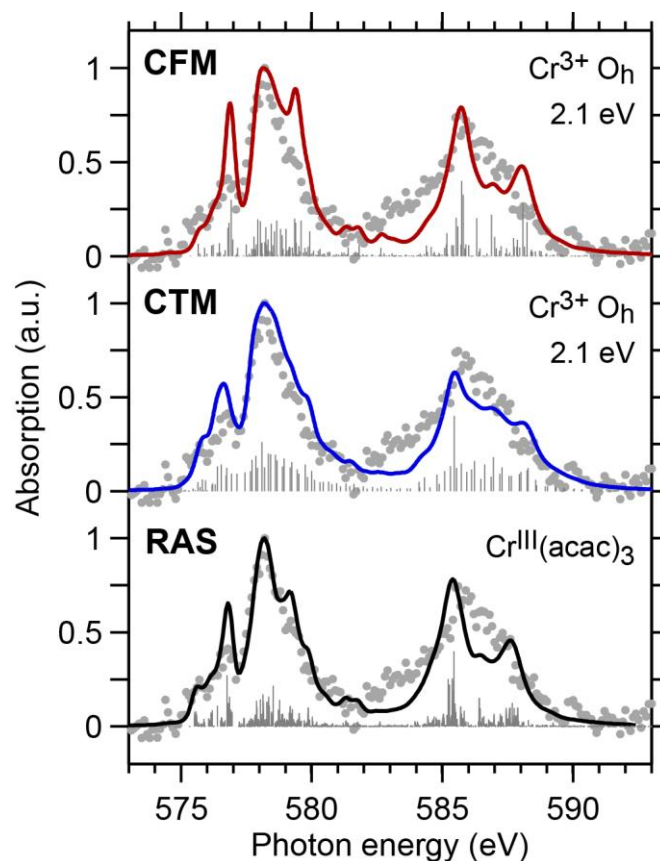


Figure 4. Comparison of the experimental Cr L-edge absorption spectrum of $\text{Cr}^{\text{III}}(\text{acac})_3$ (gray circles, taken from Fig. 3B) to calculated spectra of Cr^{3+} ($3d^3$) in octahedral coordination symmetry with $10 Dq=2.1$ eV (sticks are single transitions and solid lines are convoluted spectra). Top: Best-fitting spectrum from CFM (red, a more detailed analysis with CFM spectra can be found in the Supporting Information). Middle: Best-fitting spectrum from a CTM calculation (blue). Bottom: Calculated spectrum from ab-initio restricted active space (RAS) theory, based on the optimized molecular structure shown in Fig. 1A. The energy axes of all calculated spectra are shifted by individual energy offsets in order to match the calculated and experimental peak position in the Cr L_3 -edge.

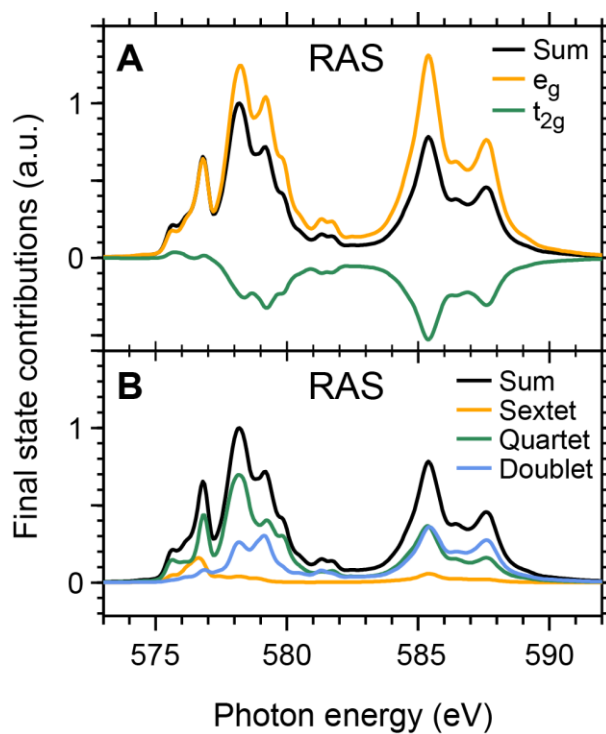


Figure 5. Decomposition of the calculated restricted active space (RAS) Cr L-edge absorption spectrum of $\text{Cr}^{\text{III}}(\text{acac})_3$ into (A): Differential orbital populations of the final core-excited states (as compared to the ground state) and (B): Spin multiplicities of the final core-excited states.

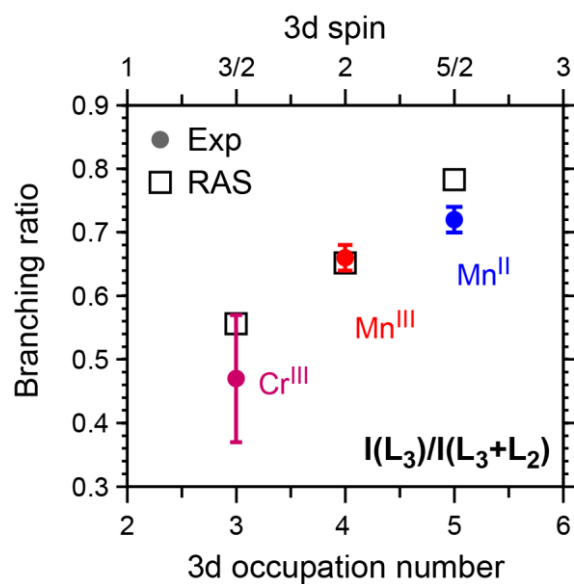


Figure 6. Comparison of measured (circles) and RAS calculated (squares) branching ratios $I(L_3)/I(L_3+L_2)$ as a function of the nominal 3d occupation number. The data for Cr^{III}(acac)₃ reported here is compared to the data of Mn^{II}(acac)₂ and Mn^{III}(acac)₃, on the basis of spectra reported in ref. 14. The error bars reflect the statistical uncertainty from scan to scan.

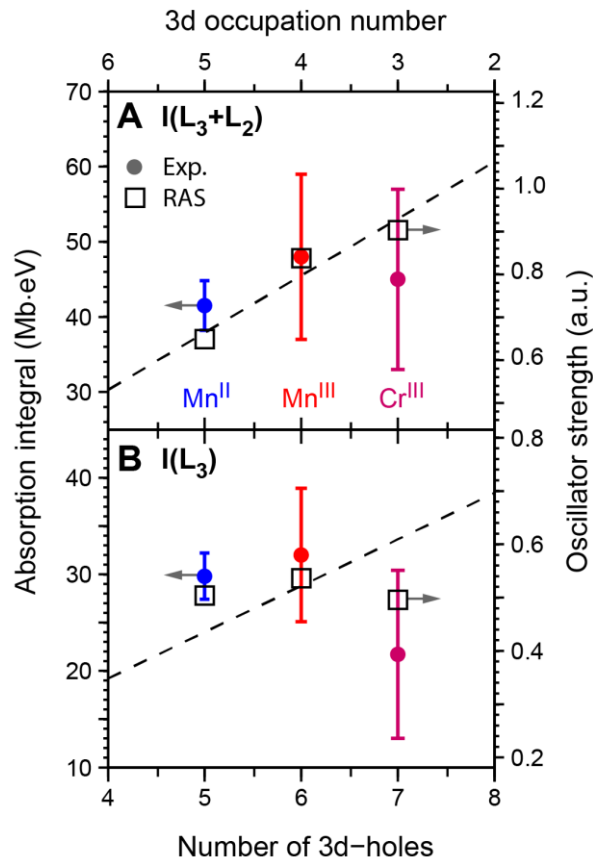


Figure 7. Comparison of measured absorption integrals (absorption cross sections integrated over respective energy ranges, see text, circles) and calculated sums of oscillator strengths from RAS (squares) for the full L-edge (A) and for the L₃-edge only (B) as a function of increasing number of nominal 3d-holes (decreasing nominal 3d occupation). Data points for Mn^{II} and Mn^{III} are used as reported in ref. 14. The dashed lines are weighted linear fits to the experimental data (forced to include the origin). A linear fit to the RAS data was used to scale the respective plot ranges of experiment and theory for coinciding fit lines.

TOC Graphic

